


# Manipulating coherent interaction of molecular vibrations with quasibound states in the continuum in all-dielectric metasurfaces

Peng Xie<sup>1</sup> and Yihan Cheng<sup>2,\*</sup>

<sup>1</sup>College of Physics, Sichuan University, Chengdu 610064, China

<sup>2</sup>International Center for Quantum Materials, School of Physics, Peking University, Beijing 100871, China

 (Received 3 May 2023; revised 26 August 2023; accepted 27 September 2023; published 10 October 2023)

Bound state in the continuum (BIC) in all-dielectric metasurfaces can strongly enhance light-matter interactions in mid-infrared range, owing to their extreme field confinement with low optical losses. The excitation of BIC thus bear potential for vibrational strong coupling (VSC) with molecules, which has rarely been studied so far. Here, we combine poly (methyl methacrylate) (PMMA) molecules with a simple all-dielectric metasurface, demonstrating the VSC between symmetry-protected BIC modes and PMMA molecular vibrations with a flexible tuning of the coupling strength. We demonstrate the strong dependence of the coupling strength on the  $Q$  factor of the quasi-BIC (QBIC) mode and achieve a large Rabi splitting up to 4.45 meV ( $67\text{ cm}^{-1}$ ), which is the maximum value reported so far in BIC-based dielectric nanostructures. A full-quantum model is utilized to fully describe the coupling dynamics of the strongly interacting system, revealing the ultrafast energy transfer between the QBIC and variational state with long coherence time. The proposed hybrid system provides a promising platform both for the fundamental study on light-matter interactions and for potential applications in high-compact nanophotonic devices in mid-infrared frequencies.

DOI: [10.1103/PhysRevB.108.155412](https://doi.org/10.1103/PhysRevB.108.155412)

## I. INTRODUCTION

Vibrational strong coupling (VSC), the strong coupling between optical excitations and molecular vibrational transitions in mid-infrared range, has drawn tremendous attention due to its fundamental importance in the study of light-matter interactions and great potential in manipulating chemical reactions and in infrared spectroscopic applications [1,2]. VSC can be achieved when the coherent energy exchange rate between optical resonators and molecules is faster than the respective dissipation rate [3–5]. The molecule polarization state formed by VSC featuring Rabi splitting is a completely different composition from the initial pure component, which is of great use for changing the potential energy distribution of molecular reactions, modifying the chemical properties of molecules and the development of ultrasensitive infrared spectroscopy devices [1,2].

In the regime of VSC, the coupling strength  $g$ , which is used to characterize the rate of energy exchange between optical resonator and molecular vibrations, can be expressed as  $\hbar g = \boldsymbol{\mu}_m \cdot \mathbf{E} \propto \mu_e \sqrt{\hbar \omega / \epsilon V}$ , where  $\mu_m$ ,  $\epsilon$ ,  $\omega$ ,  $V$  represent transition dipole moment of the molecule, the dielectric constant, the excitation frequency, and the optical mode volume, respectively [6–9]. The Rabi splitting  $\Omega_R$  induced by strong coupling is given as  $\Omega_R = \sqrt{4g^2 - (\kappa - \gamma_m)^2}/4$ , where  $\kappa$  and  $\gamma_m$  represent the photon leakage rate of the optical modes and damping rates of molecular excitation, respectively. Therefore, increasing  $g$  or decreasing the difference between  $\kappa$  and  $\gamma_m$  is the most direct way to achieve the Rabi splitting, which

can be easily accessed and evaluated in far-field spectroscopic measurements.

To reach VSC, molecular transitions have been used to couple with cavity-based photonic resonators, such as whispering gallery cavities, microwave cavities, and Fabry-Perot cavities [2,10–12], or with plasmonic nanostructures supporting various types of plasmonic excitations. The cavity-based structures can support high  $Q$  factors (small  $\kappa$ ) and simultaneously excite different orders of optical resonance, which facilitates strong coupling or even collective ultrastrong coupling with molecular excitation. However, such devices are usually designed with relative bulky geometries for practical convenience [13]. Moreover, shrinking such photonic and plasmonic resonators down to the micro- or nanoscale to enhance VSC is still challenging due to the low field enhancement of photonic modes or the large mode volume of plasmonic resonances at mid-infrared frequencies.

An alternative way of enhancing VSC is to employ surface phonon polaritons (SPhPs) supported by two-dimensional (2D) materials [4,14] or polar crystals [15–19]. SPhPs, as the quasiparticles formed by the mixture of photons with optical phonons, exhibit pronounced polaritonic dispersion with low optical losses. They allow a deep field squeezing down to subdiffractional level at mid-infrared frequencies with greatly enhanced field strength and picosecond-long lifetime [20–22]. Recently, VSC has been observed between molecular vibrations and SPhPs in a hexagonal boron nitride flake and SiO<sub>2</sub> single nanopillars [3]. Pronounced mode splitting and anticrossing dispersion were observed in the far-field reflectivity spectra at mid-infrared frequencies.

Other than SPhP resonance, strong electromagnetic field enhancement and confinement can also be achieved in

\*yhcheng@pku.edu.cn

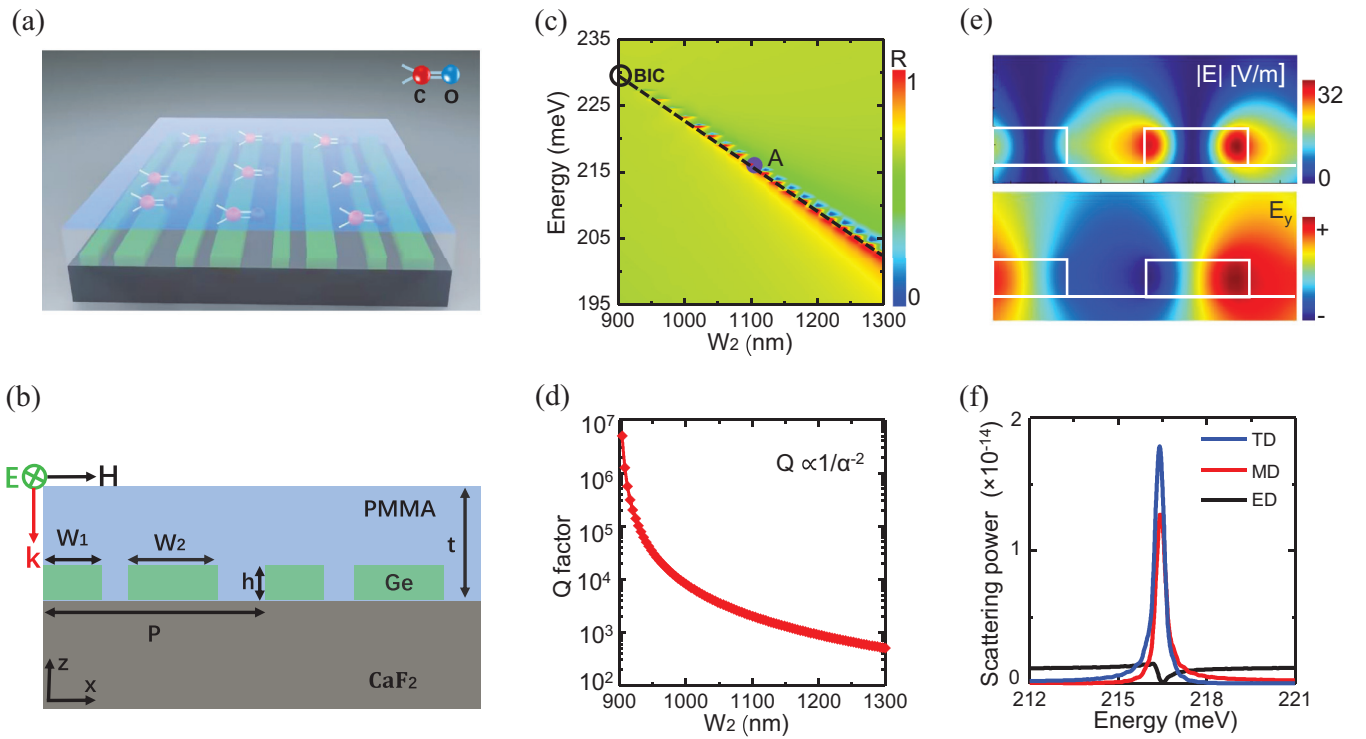


FIG. 1. (a) Three-dimensional schematic of the coupling system. (b) Parameter layout of the hybrid system in the  $x$ - $z$  plane: period  $P = 3400$  nm, width of Ge grating  $W_1 = 900$  nm,  $W_2 = 900$ – $1300$  nm, height  $h = 400$  nm, thickness of PMMA  $t = 0$ – $800$  nm. (c) Simulated reflection spectra with different width  $W_2$ . (d)  $Q$  factor of the QBIC mode as a function of the asymmetric parameter  $\alpha$ . (e) The amplitude (top) and  $y$  component of the electric field distributed in  $z$ - $x$  plane at QBIC resonance [Point A in (c)]. (f) Scattering power of different dipole moments calculated in Cartesian coordinate system. ED, MD, TD represent the electric, magnetic, and toroidal dipole moment, respectively.

mid-infrared range via bound states in the continuum (BIC). BIC is a leaky mode with infinite quality factor ( $Q$  factor) within the continuous background spectrum. Only in the past decade their rich physics has been employed to engineer sharp resonances (high- $Q$  factors) in the form of quasi-BIC (QBIC) in a variety of dielectric photonic systems [23–25]. Supported by subwavelength dielectric particles, QBIC provide an efficient light trapping inside the particle volumes with very low optical losses, thus offering an alternative platform for studying light-matter interactions [26–29]. The QBIC modes combine strong light capture capability, flexible tuning (shape, size, and asymmetry changes), and rich optical mode excitation (electric, magnetic, and toroidal modes, etc.), which provides a possibility to realize customized QBIC mode interactions with molecular excitations [24]. So far, most research has focused on the strong coupling of QBIC modes with excitonic resonances in transition-metal dichalcogenides (TMDs), perovskite, and molecular excitations in the optical band [23,25,30–36]. However, strong coupling between molecular vibrations and QBIC modes supported by all-dielectric metasurfaces in the mid-infrared band has rarely been reported [34]. In particular, manipulating VSC coupling strength with flexible tunability in QBIC-based hybrid systems has not been studied, which is expected to be of great importance both for fundamental physics of light-matter interactions in mid-infrared range and for potential applications in metasurface-based ultracompact nanophotonic devices working at mid-infrared frequencies.

In this paper, we investigate the VSC between symmetry-protected QBIC modes and poly (methyl methacrylate) (PMMA) molecular vibrations through an asymmetric germanium (Ge) grating covered by PMMA molecular layers. We demonstrate a flexible weak-to-strong tuning of the coupling between QBIC and molecular vibrations by modulating the PMMA molecular layer thickness. We demonstrate the strong dependence of the coupling strength on the  $Q$  factor of the QBIC mode, which offers an effective way of achieving enhanced coupling strength. An optimal structural design enables a large VSC Rabi splitting up to  $4.45$  meV ( $67$   $\text{cm}^{-1}$ ), which is the maximum value reported so far in BIC-based dielectric nanostructures. Importantly, a full-quantum model is employed to give a full description of the coupling dynamics of the strongly interacting system, revealing the ultrafast energy transfer between the QBIC and vibrational state with long coherence time. The proposed hybrid system provides a promising platform both for the fundamental study on light-matter interactions and for potential applications in high-compact nanophotonic devices in mid-infrared frequencies.

## II. RESULTS AND DISCUSSION

### A. The strong coupling system

The proposed hybrid system, as shown in Fig. 1(a), contains an asymmetric Ge grating on  $\text{CaF}_2$  substrate, with the grating structure completely covered by a PMMA molecular layer. Here, we focus on the interaction between the

QBIC mode and the C=O bond resonance ( $1730\text{ cm}^{-1}$ ) in the PMMA molecules in the present system. We calculated the reflection spectrum of the coupled system as a function of the width  $W_2$  using the finite difference time domain (FDTD). In our simulation, a TE wave with E field oscillating along  $y$  direction is used to illuminate the grating structure at normal incidence, as shown in Fig. 1(b). Periodic boundary conditions are employed in  $x$  and  $y$  direction of the unit cell, while a perfect matching layer (PML) condition is used in  $z$  direction. We divide the mesh of the simulation area into  $1 \times 1 \times 1\text{ nm}$  to ensure the accuracy of the calculation results. The refractive indices of  $\text{CaF}_2$  and Ge were set to  $n_{\text{CaF}_2} = 1.4$  and  $n_{\text{Ge}} = 4.007$ , respectively. For the C=O bond resonance of the PMMA molecule, we can describe it by the classical Lorentz oscillator as [37–39]

$$\epsilon_{\text{PMMA}} = \epsilon_B + \frac{f_0 \omega_0^2}{\omega_0^2 - \omega^2 - i\omega\gamma_0}, \quad (1)$$

where  $\epsilon_B = 2.2$  is the background permittivity in the high-frequency region.  $f_0 = 0.018$ ,  $\omega_0 = 3.253 \times 10^{14}\text{ rad/s}$  and  $\gamma_0 = 5 \times 10^{12}\text{ rad/s}$  represent the oscillator strength, the Lorentz resonance frequency, and damping constant giving the Lorentzian dispersion, respectively.

We first calculated the reflection spectrum of the nanosystem as a function of the width  $W_2$  by considering only the case where the Ge grating is completely covered by the PMMA background index-only material. The difference between widths  $W_1$  and  $W_2$  realizes a symmetric breaking in the  $x$ - $y$  plane and releases the radiation channel, which leads to the symmetric protected BIC to QBIC transition, as shown in Fig. 1(c). It is remarkable that the Ge grating excites a completely nonradiative BIC mode (infinite  $Q$  factor) around  $229\text{ meV}$  when the width  $W_2 = 900\text{ nm}$ . The QBIC resonance with finite  $Q$  factor gradually redshifts through the scanning width  $W_2$  from  $900$  to  $1300\text{ nm}$ . Figure 1(d) gives the  $Q$  factor of the QBIC resonances as a function of the asymmetric parameter  $\alpha$ , which is defined as  $\alpha = (W_2 - W_1)/W_1$ . We find that the  $Q$  factor follows exactly the typical quadratic inverse law of QBIC mode for symmetry-breaking designs, i.e.,  $Q \propto 1/\alpha^{-2}$  [40]. The  $Q$  factor of the resonance can be manipulated by adjusting the asymmetric parameter of the nanostructure, which offers an efficient way of tuning the coupling strength  $g$  of the hybrid system, as will be discussed in detail in a later section.

In order to have a deep understanding of the optical properties of the current QBIC mode, we simulated the electric field distribution of the peak A identified in Fig. 1(c), as shown at the top of Fig. 1(e). We note that the nanosystem achieves up to 32-fold enhancement of the electric field intensity compared to the incident light field, which is comparable to the field enhancement capability of plasmonic nanostructures. It is known that the total coupling strength  $\hbar g$  is the summation of the coupling strength  $g_i(r)$  of the individual quantum emitters involved in the coupling, i.e.,  $g = \sum g_i(r) = \mu \cdot \mathbf{E}_i(\mathbf{r})$ , therefore, the large electromagnetic field enhancement of the current QBIC mode accounts for the increase of the coupling strength. In addition, we also calculated the electric field distribution in the  $y$  direction within the cell, as shown at the bottom of Fig. 1(e). The electric field distribution in the  $y$

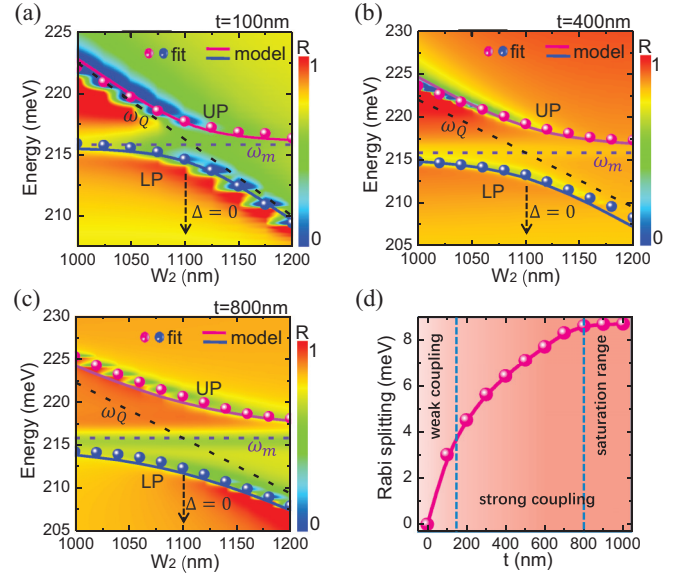


FIG. 2. Reflection spectra of different coupled systems: (a) weak coupling system; (b) strong coupling system; (c) saturation coupling system. The dispersion relations of different coupling systems are obtainable by fitting the simulated reflection spectra (sphere) and model (solid lines), respectively. The black dashed line and purple dashed line represent the resonant energy of QBIC mode and PMMA, respectively. (d) Rabi splitting as a function of PMMA thickness  $t$ .

direction exhibits an antisymmetric property, which greatly reduces the energy loss of the nanosystem. We also quantitatively analyzed the properties of multipoles of the QBIC mode by multipolar expansion method [41,42], as shown in Fig. 1(f). Figure 1(f) shows the scattering power of the electric dipole (ED), the magnetic dipole (MD), and the toroidal dipole (TD), respectively, indicating that the current resonant mode is the TD-dominated QBIC mode.

## B. QBIC mode coupled with PMMA molecular vibration

In this section, we will investigate in detail the interaction between QBIC and PMMA and the manipulation of the coupling strength. Figures 2(a)–2(c) give the reflection spectrum as a function of width  $W_2$  for PMMA with thickness  $t = 100\text{ nm}$ ,  $t = 400\text{ nm}$ , and  $t = 800\text{ nm}$ , respectively, which correspond to Ge gratings not covered, just covered, and completely covered by PMMA layers, respectively. It is remarkable to note the anticross behavior in all three cases, which indicates a coherent interaction between the QBIC mode and the PMMA molecule.

To obtain the spectral property of the coupling system, we extracted the dispersion relationship and linewidth features of the polariton induced by the coupling through Fano-shaped line fitting of the simulated reflectance spectra. The reflectance spectrum  $R(\omega) = |r(\omega)|^2$  can be expressed as [43,44]

$$t(\omega) = a_b + \sum_{j=\text{UP,LP}}^N \frac{b_j \gamma_j e^{i\phi_j}}{\omega - \omega_j + i\gamma_j}, \quad (2)$$

where  $a_b$ ,  $b_j$ , and  $\phi_j$  represent the background amplitude, amplitude, and the phase of the reflectance spectrum, respectively.  $\omega_j$  and  $2\gamma_j$  are the dispersion and the reflectance spectrum full width at half maximum (FWHM) of upper polariton (UP) and lower polariton (LP) modes. The dispersion relationship (pink sphere: UP; blue sphere: LP) extracted by fitting can perfectly reproduce the three current simulated reflectance spectra. Thus the Rabi splitting  $\hbar\Omega$  of the hybrid system at zero detuning ( $\omega_{\text{QBIC}} = \omega_m$ ), which is the physical quantity characterizing the energy exchange between the two subsystems, can be roughly estimated by the difference between the UP and LP resonance energies. We finally calculate the Rabi splitting for the three coupling systems in Figs. 2(a)–2(c) corresponding to 2.85 meV, 6 meV, and 8.6 meV, respectively. Importantly, we also found a redundant peak gradually appearing between the UP and LP resonance peaks as the thickness of the PMMA layer increases, indicating that some molecular vibrations are not involved in the coupling. This peculiar phenomenon will be described in the next section by a full-quantum model.

To quantitatively describe the coherent coupling properties between QBIC modes and PMMA molecules, the interaction process is described by the widely used coupled oscillator model (COM), as follows [45]

$$\hbar \begin{pmatrix} \omega_Q - i\gamma_Q & g \\ g & \omega_m - i\gamma_m \end{pmatrix} \begin{pmatrix} \alpha \\ \beta \end{pmatrix} = \hbar\omega_{\pm} \begin{pmatrix} \alpha \\ \beta \end{pmatrix}, \quad (3)$$

where  $\tilde{\omega}_Q = \omega_Q - i\gamma_Q$  and  $\tilde{\omega}_m = \omega_m - i\gamma_m$  are the complex resonance frequencies of QBIC mode and PMMA molecular vibration, respectively.  $\alpha$  and  $\beta$  represent the components of the eigenvectors, which satisfies the relation  $|\alpha|^2 + |\beta|^2 = 1$ . It should be noted that Eq. (3) is only applicable to the above coupled system with PMMA layer thicknesses of  $t = 100$  nm [Fig. 2(a)] and  $t = 400$  nm [Fig. 2(b)]. Since some of the molecular vibrations are not involved in the coupling process for a coupling system with the PMMA layer thickness of  $t = 800$  nm [Fig. 2(c)], the COM should be constructed as follows

$$H = \hbar \begin{pmatrix} \omega_Q - i\gamma_Q & g & 0 \\ g & \omega_m - i\gamma_m & 0 \\ 0 & 0 & \omega_r - i\gamma_r \end{pmatrix}, \quad (4)$$

where  $\omega_r = \omega_m$  and  $\gamma_r$  are the frequencies and FWHM of redundant molecular vibrations, respectively. By diagonalizing Eq. (3) or Eq. (4), the dispersion relationship of the polariton modes can be obtained as

$$E_{\pm} = \hbar\omega_{\pm} = \frac{\hbar}{2} [(\omega_Q + \omega_m - i\gamma_X - i\gamma_m) \pm \sqrt{4g^2 + [\omega_Q - \omega_m - i(\gamma_m - \gamma_Q)]^2}]. \quad (5)$$

With the system at zero detuning condition, the coupling strength  $\hbar g$  is calculated as

$$\hbar g = \frac{\hbar}{2} \sqrt{\Omega^2 + (\gamma_m - \gamma_Q)^2}. \quad (6)$$

To determine whether the coupled system is in the strong coupling range, it must satisfy the following two

criteria:

$$g > |\gamma_m - \gamma_Q|/2, \quad (7)$$

$$g > \sqrt{(\gamma_m^2 + \gamma_Q^2)}/2. \quad (8)$$

Equation (7) guarantees the existence of Rabi splitting, and Eq. (8) is to ensure that Rabi splitting can be verified experimentally.

For the coupling system with PMMA layer thicknesses  $t = 100$  nm,  $t = 400$  nm, and  $t = 800$  nm, we fit the reflection spectrum of the uncoupled QBIC mode according to Eq. (2) and obtain the damping rate  $\hbar\gamma_Q$  as 0.16 meV, 0.19 meV, and 0.23 meV, respectively. The damping constant  $\hbar\gamma_m$  of PMMA molecules is 3.28 meV. Therefore, the coupling strengths  $\hbar g$  for the corresponding hybrid systems in Figs. 2(a)–2(b) were calculated by Eq. (6) as 2.13 meV and 3.37 meV, respectively. For the coupling system in Fig. 2(c), the damping rate  $\hbar\gamma_r$  of the uncoupled molecular vibrations was determined as 0.75 meV by fitting the spectrum at zero detuning, which leads to the damping rate  $\hbar\gamma_m$  of the PMMA molecules involved in the coupling being determined as  $\hbar\gamma_m = 3.28 \text{ meV} - \gamma_r = 2.53 \text{ meV}$ . We finally calculated the coupling strength  $\hbar g$  of the hybrid system in Fig. 2(c) as 4.45 meV. In addition, we also obtain the dispersion of the hybrid states (solid pink line: UP; solid blue line: LP) of the corresponding coupled system by bringing the above coupling strengths  $\hbar g$  into Eq. (3) or Eq. (4), which perfectly reproduce the dispersion obtained by fitting, as shown in Figs. 2(a)–2(c). Based on the determination Eqs. (7) and (8), we identify the coupling system in Fig. 2(a) as a weak coupled system, while the systems in Figs. 2(b)–(c) are in the strong coupling regime.

Furthermore, the Rabi splitting  $\hbar\Omega$  as a function of PMMA layer thickness  $t$  is given in Fig. 2(d). Obviously, as the thickness of PMMA layer increases, the Rabi splitting value gradually increases and eventually reaches the saturation state, which is attributed to the gradual increase of molecular vibrations involved in the coupling process. We found that: (i) the system is in the weak coupling region when the PMMA layer thickness  $t$  is below 140 nm, and importantly (ii) the system reaches saturation when the PMMA layer thickness  $t$  is above 800 nm. We can easily control the coupling strength of the system with flexible tunability by altering the number of molecules involved in the coupling.

### C. Quantum model description of the coupling process

It is essential to study the unique coupling dynamics for systems with light-matter interactions, especially for the hybrid systems that are currently in saturation, which is of great importance for the study of quantum optical effects. In this section, we construct a full quantum model under the Heisenberg-Langevin framework to quantitatively describe the spectral response and the ultrafast dynamics of the QBIC-PMMA system in continuum reservoirs. Note that we only show here the spectral response and coupling dynamics of the QBIC-PMMA strongly coupled system. The hybrid system in Fig. 2(b) can be regarded as an interaction between a fermionic system and a bosonic system. The coupled system in Fig. 2(c) can be considered as the interaction between two fermionic systems and a bosonic subsystem. The total Hamil-

tonian can be expressed as  $H = H_F + H_I + H_D + H_R + H_S$ , where  $H_F$  [46–49],  $H_I$ ,  $H_D$ ,  $H_R$ ,  $H_S$  represent the Hamiltonian terms for subsystems, interaction terms between subsystems, interaction terms between subsystems and excitation fields, radiation and dissipation process terms from subsystems to continuous medium reservoirs, and interaction terms between subsystems and continuous medium reservoirs, respectively. The specific form of each Hamiltonian term can be found in the Appendix.

A standard genetic algorithm was used to search for possible parameters to match the reflectance spectrum of the simulated coupled system in a prescribed reasonable parameter space. We finally obtained the coherent coupling strength  $\hbar g$  and incoherent coupling strength  $\hbar \gamma$  for the coupled system of Fig. 2(b) as  $\hbar g = 3.37$  meV and  $\hbar \gamma = -0.15$  meV, respectively. The coherent and incoherent coupling strengths of the coupled system of Fig. 2(c) are optimized as  $\hbar g = -4.45$  meV and  $\hbar \gamma = 0.2$  meV, respectively. Here we assume that the coherent coupling strengths of both the redundant PMMA molecular vibration—QBIC mode (coupling strength:  $\hbar g_{rQ}$ ), and the redundant PMMA molecular vibration—other molecular vibrations (coupling strength:  $\hbar g_{rm}$ ) in the coupling system of Fig. 2(c) are 0 meV. It is remarkable that the coherent coupling strengths of the coupled systems in Figs. 2(b) and 2(c) have different signs, which are attributed to the initial phase  $\phi$  difference between the two subsystems. This results in a coupling strength of the hybrid system that is usually a complex quantity, i.e.,  $\hbar g = \hbar |g| e^{i\phi}$ . Therefore, we can deduce that the Rabi phase  $\phi$  of the hybrid system in Fig. 2(b) is  $0^\circ$ , while the Rabi phase  $\phi$  of the coupled system in Fig. 2(c) is  $180^\circ$ . The underlying physics of the reverse of Rabi phase for different coupling strength can be explained as the phase change of the reemitted electric field of vibrational molecules with respect to that of QBIC mode, which originates from the increase of the thickness of the PMMA film. This reverse of Rabi phase does not change the coherent coupling strength of the system, but play an important role in determining the spectral profile of the polariton modes, thus offering a promising approach for manipulating the spectral amplitude of the hybrid states. The incoherent coupling strength is induced by coherent coupling, specifically in the form of the release of photons from one system through a continuous medium reservoir being reabsorbed by another subsystem, which ultimately leads to sub- and super-radiation phenomena [43,50].

With the above optimized coherent and incoherent coupling strengths as input parameters, we finally obtained the reflection spectrum as a function of width  $W_2$  under the Heisenberg-Langevin framework, as shown in Fig. 3(a) and Fig. 3(b). In addition, we fitted its reflection spectrum by Eq. (2) to extract the dispersion relationship (UP: pink solid line; LP: blue solid line) of the polariton states. The reflection spectra and dispersion obtained by quantum models and simulations are consistent, demonstrating the VSC between QBIC modes and PMMA molecular vibrations. In particular, we have succeeded here in constructing a quantum model in which only some of the molecular vibrations are involved in the coupling process, which provides ideas for extension to other systems. We also present the real-time population dynamics of the UP states of the two coupled systems on

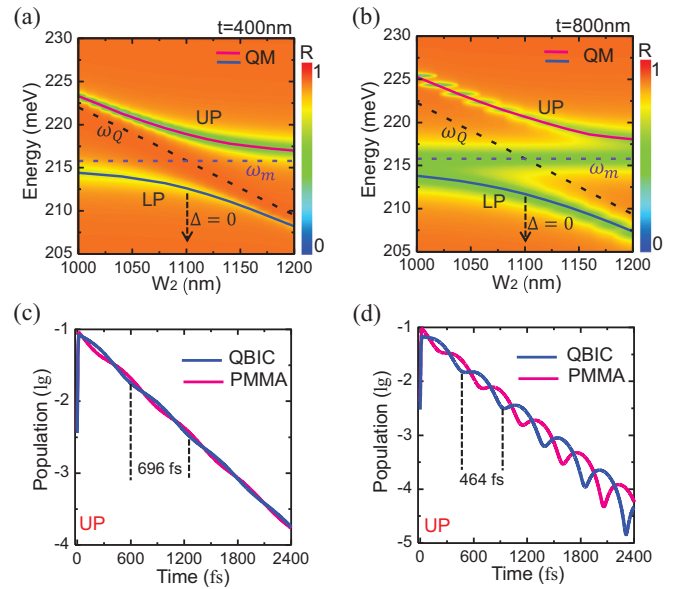


FIG. 3. The reflection spectra calculated by quantum model for different coupled systems. (a) strong coupling systems, (b) saturated coupling systems. Time-domain evolution of the QBIC (blue solid line) and PMMA (pink solid line) population in the UP polarization state of strong coupling system (c) and saturated coupling system (d).

a logarithmic scale, as shown in Figs. 3(c) and 3(d). The energy exchange between the QBIC mode and the PMMA molecular vibrations is observed with periods characterized by Rabi oscillations. The Rabi periods of the two coupled systems were determined to be  $T = 696$  fs and  $T = 464$  fs, respectively. Note that the energy exchange of the strong coupling system is more intense in the saturated state, which is attributed to the involvement of more molecular vibrations in the coupling process. Importantly, the population transfer between the two subsystems can persist over eight Rabi cycles, corresponding to a surprisingly long coherence time over several picoseconds. This is in contrast to other observations in strongly coupled plasmon, or cavity modes coupled with excitonic resonances, in which larger Rabi oscillations occur in the range of femtoseconds with coherence times shorter than several tens of femtoseconds. Such shorter coherence times were mainly attributed to the broad plasmon/cavity linewidth due to strong radiative and nonradiative damping [51–53]. While in the present BIC-based system, the spectral width of QBIC is tuned to be comparable to that of the molecular resonance. The spectral width of QBIC is generally narrow and only determined by its small leakage rate. Therefore, the hybrid system exhibits very strong coupling energy with ultrafast energy exchange rate and prolonged coherence time. Such unique dynamics of the coupled system is of great importance for future applications in realizing all-dielectric metasurface-based quantum devices.

#### D. Manipulation of coupling strength

In this section, we will investigate the way of controlling the coupling strength in the hybrid system by tuning the  $Q$  factor of the QBIC mode. It has been demonstrated that the  $Q$  factor of the QBIC mode is strongly dependent on the

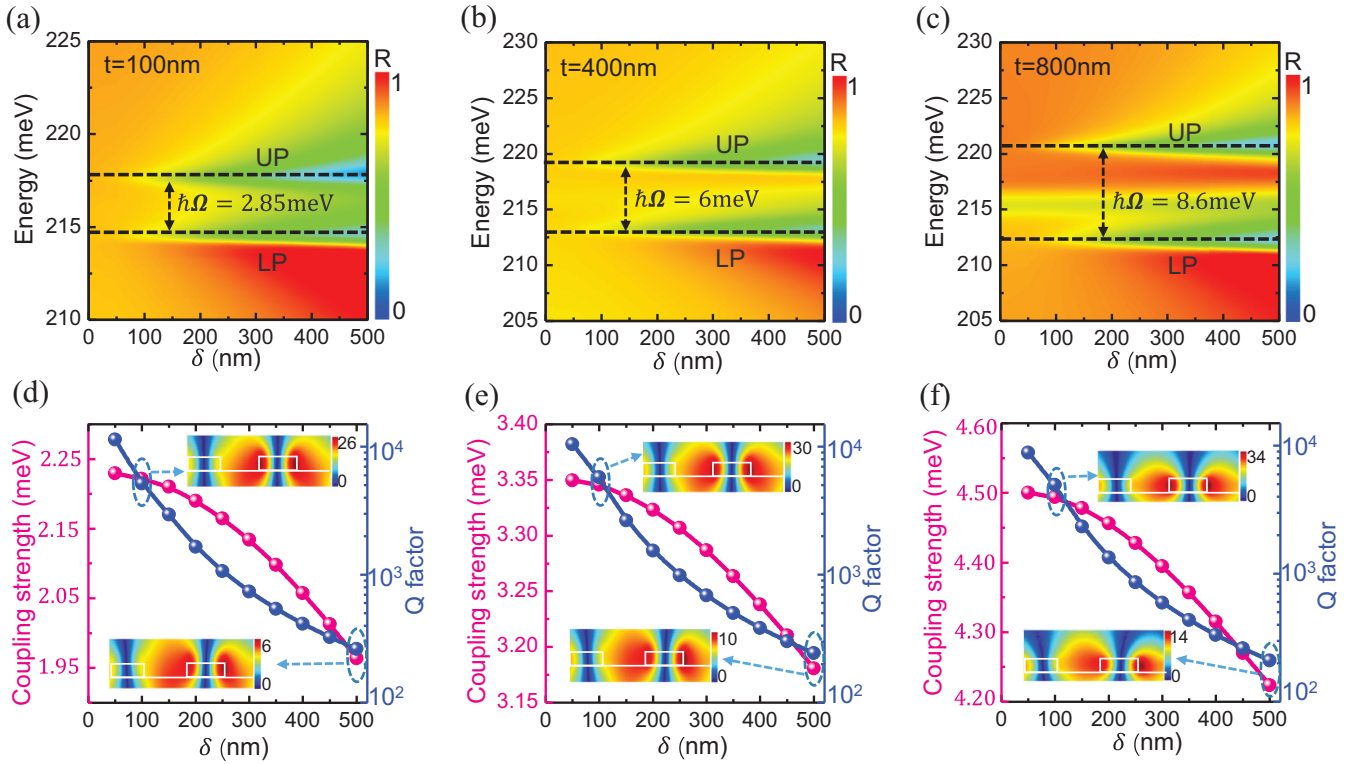


FIG. 4. The simulated reflection spectra of different coupling systems as a function of the slit difference  $\delta$ : (a) weak coupling system, (b) strong coupling system, (c) saturated strong coupling system. Coupling strength  $g$  and  $Q$  factor for different coupling systems as a function of the slit difference  $\delta$ : (d) weak coupling system; (e) strong coupling system; (f) saturation coupling system. The inset shows the electric field distribution for the slit difference  $\delta = 100$  nm and  $\delta = 500$  nm, respectively.

asymmetric parameters. It can also be arbitrarily adjusted by other parameters of the grating structure. Here, we change the position of the Ge bar (marked with width  $W_2$ ) with respect to the other Ge bar (marked with width  $W_1$ ) while keeping the other parameters fixed. The difference in slit width of the Ge grating is defined as  $\delta$ . The simulated reflection spectra as a function of  $\delta$  for the coupling system for PMMA layer thicknesses  $t=100$  nm,  $t=400$  nm, and  $t=800$  nm are given in Figs. 4(a)–(c), respectively. We found that the resonant frequencies of UP and LP were not shifted, which implies that their energy difference, i.e., the Rabi splitting  $\hbar\Omega$ , was constant. This is different from the results demonstrated in Ref. [54], in which the difference of the spectral width of the two subsystems is sufficiently large so that the Rabi splitting estimated from the reflection spectra varies dramatically as the  $Q$  factor of the QBIC resonance increases. While in our present case, the spectral widths of the two subsystems are carefully designed to be comparable. In this sense, we enabled a flexible tuning of coupling strength while keeping a constant Rabi splitting [Figs. 4(a)–(c)]. Such unique property of the strongly coupled system is beneficial for the future applications in ultracompact infrared functional devices due to its high tunability with excellent robustness.

Subsequently, we give the evolution trend of the coupling strength  $g$  (pink spheres) with the parameter  $\delta$  based on Eq. (6). It is found that the coupling strength gradually decreases as  $\delta$  increases. To analyze the physical mechanism behind this, we extracted the  $Q$  factor of the QBIC mode,

as shown in Fig. 4(e)–4(f) (blue spheres). We also calculated the electric field distribution in the cell corresponding to the QBIC modes with high and low  $Q$  factors, as shown in the inset in Figs. 4(e)–4(f). It can be observed that the electric field strength gradually decreases as the  $Q$  factor decreases, which means that the electromagnetic energy stored in the QBIC mode is sharply reduced. This leads to a gradual decrease in the coupling strength of the hybrid system, as it is known that the coupling strength  $g$  greatly depends on the field enhancement of the nanostructure. The property will provide convenience for the purpose of enhancing the coupling strength, such as reducing the difference between the slits of the Ge gratings.

### III. CONCLUSIONS

To conclude, we have investigated the VSC between symmetry-protected BIC modes and PMMA molecular vibrations in the hybrid system containing an asymmetric Ge grating covered by PMMA molecular layers. By modulating the PMMA molecular layer thickness, we have demonstrated a flexible weak-to-strong tuning of the coupling between QBIC and molecular vibrations. The strong dependence of the coupling strength on the  $Q$  factor of the QBIC mode provides an effective way of achieving enhanced coupling strength. A large VSC Rabi splitting up to 4.45 meV have been achieved with an optimal structural design. Importantly, a full-quantum model has been employed to give a full description of the cou-

pling dynamics of the strongly interacting system, revealing the ultrafast energy transfer between the QBIC and variational state with long coherence time. The proposed hybrid system provides a promising platform both for the fundamental study on light-matter interactions and for potential applications in high-compact nanophotonic devices in mid-infrared frequencies.

### ACKNOWLEDGMENTS

This work was supported by the National Natural Science Foundation of China (Grant No. 11974254).

### APPENDIX: DETAILS FOR HEISENBERG-LANGEVIN FORMALISM IN COUPLING SYSTEM

We construct a full-quantum model to quantitatively analyze the microscopic dynamics of the interaction between QBIC and molecular vibrations in the Heisenberg-Langevin formalism. The resonant frequencies of QBIC mode and molecular vibration are  $\omega_Q$  and  $\omega_m$ , respectively. For simplicity, the molecules involved in the coupling and the surplus molecules are distinguished by separate corner labels  $i$  ( $i = 1, 2$ ) in the latter part. Therefore, the Hamiltonian quantity of the subsystem can be expressed as

$$H_F = H_Q + H_m = \hbar\omega_Q(\hat{a}^\dagger\hat{a} + \frac{1}{2}) + \frac{1}{2}\hbar\omega_m\sigma_{iz}. \quad (\text{A1})$$

Here,  $H_Q$  is the Hamiltonian of QBICs mode, which is represented by the quantized bosonic creation (annihilation) operators  $\hat{a}^\dagger(\hat{a})$  with resonances frequency  $\omega_q$ .  $H_m$  is the Hamiltonian of molecular vibration with  $\sigma_{iz} = [\sigma_{i+}, \sigma_{i-}]$ , where  $\sigma_{i+}$  and  $\sigma_{i-}$  represent the rising and lowering operators of the fermionic system, respectively.

The interaction Hamiltonian under the rotating-wave approximation (RWA) can thus be expressed as  $H_I = \hbar(g_i\hat{a}^\dagger\sigma_{i-} + g_i^*\sigma_{i+}\hat{a})$ , where the  $g$  is the coupling strength between subsystems.

Subsequently, the Hamiltonian  $H_D$  of the interaction between subsystems and the external time-harmonic field under the excitation of the external time-harmonic field can be written  $H_D = i\hbar\sqrt{\Gamma_Q}(A_Q\hat{a}^\dagger e^{-i\omega t} - A_Q^*\hat{a}e^{-i\omega t}) + i\hbar(A_i\sigma_{i+}e^{-i\omega t} - A_i^*\sigma_{i-}e^{-i\omega t})$ .  $\Gamma_Q$  is damping rate of the QBIC.  $A_Q$  and  $A_i$  represent the interaction coefficient of subsystems to the external driving field.

Intuitively, the radiation and dissipation processes of the subsystems to the continuum reservoir can be written as  $H_R = \int \hbar\omega'(\hat{b}_\omega^\dagger\hat{b}_\omega + \hat{c}_\omega^\dagger\hat{c}_\omega)d\omega'$ . The interactions between contin-

uum reservoir and subsystems are expressed as

$$H_S = i\hbar \int (B_Q\hat{b}_\omega^\dagger\hat{a} + C_Q\hat{c}_\omega^\dagger\hat{a} + B_i\hat{b}_\omega^\dagger\sigma_{i-} + C_i\hat{c}_\omega^\dagger\sigma_{i-})d\omega' + \text{H.c.} \quad (\text{A2})$$

Here, the bosonic operator  $\hat{b}_\omega^\dagger$  with interacting coefficients  $B_Q/B_i$  are the continuum output radiative modes.  $\hat{c}_\omega^\dagger$  with coefficients  $C_Q/C_i$  represents the continuous phononic modes. The total Hamiltonian can be written as  $H = H_F + H_I + H_D + H_R + H_S$ . Thus, the time evolution of any operator  $\hat{O}$  follows the Heisenberg equations of motion, which can be expressed as

$$\begin{aligned} \dot{\hat{a}}_Q &= -i\omega_Q\hat{a} - ig_i\sigma_{i-} + \sqrt{\Gamma_Q}A_Qe^{-i\omega t} \\ &\quad - B_Q \int b_\omega d\omega' - C_Q \int c_\omega d\omega', \\ \dot{\hat{b}}_{\omega'} &= -i\omega'b_{\omega'} + B_Q\hat{a}_q + B_i\hat{a}_c, \\ \dot{\hat{c}}_{\omega'} &= -i\omega'c_{\omega'} + C_Q\hat{a}_q + C_i\hat{a}_c, \\ \dot{\sigma}_{i-} &= -i\omega_i\sigma_{i-} + ig_i^*\sigma_{iz}\hat{a} - A_i\sigma_{iz}e^{-i\omega t} \\ &\quad + \sigma_{iz} \left( \int B_i b_\omega d\omega' + \int C_i c_\omega d\omega' \right), \\ \dot{\sigma}_{iz} &= 2i(g_i\hat{a}^\dagger\sigma_{i-} - g_i^*\sigma_{i-}\hat{a}) + 2\Omega_i(\sigma_{i+}e^{-i\omega t} + \sigma_{i-}e^{i\omega t}) \\ &\quad - 2 \int (B_i\hat{b}_\omega^\dagger\sigma_{i-} + C_i\hat{c}_\omega^\dagger\sigma_{i-} + \text{H.c.})d\omega', \end{aligned} \quad (\text{A3})$$

Integrating  $\hat{b}_\omega'$  and  $\hat{c}_\omega'$  in time yields

$$\begin{aligned} \hat{b}_{\omega'}(t) &= \hat{b}_{\omega'}(0)e^{-i\omega't} + \int_0^t (B_Q\hat{a} + B_i\sigma_{i-})e^{-i\omega'(t-t')}dt', \\ \hat{c}_{\omega'}(t) &= \hat{c}_{\omega'}(0)e^{-i\omega't} + \int_0^t (C_Q\hat{a} + C_i\sigma_{i-})e^{-i\omega'(t-t')}dt'. \end{aligned}$$

The relationship between the damping rate of the subsystem and the interaction coefficient can be related by  $\Gamma_k = 2\pi(B_k^2 + C_k^2) \equiv 2\gamma_k$  ( $k = q, l$ ). The incoherent damping channel characterized by incoherent coupling coefficients can be expressed as  $\gamma_{kl}$ , i.e.,  $\Gamma = 2\pi(B_QB_i + C_QC_i) \equiv 2\gamma_i$  [47,48,51].

Under weak-pump approximation, we can obtain

$$\begin{aligned} \dot{\hat{a}} &= -(i\Delta_Q + \gamma_Q)\hat{a} - (ig_i + \gamma_{Qi})\sigma_{i-} + \sqrt{\Gamma_Q}A_Q + \hat{F}_Q, \\ \dot{\sigma}_{i-} &= -(i\Delta_i + \gamma_i)\sigma_{i-} - (ig_i^* + \gamma_{Qi})\hat{a} - A_Q\sigma_{iz} + \hat{F}_i. \end{aligned} \quad (\text{A4})$$

Therefore, the steady-state solution and real-time dynamics of the coupled system can be obtained by solving Eq. (A4).

- [1] A. Thomas, L. Lethuillier-Karl, K. Nagarajan, R. M. A. Vergauwe, J. George, T. Chervy, A. Shalabney, E. Devaux, C. Genet, J. Moran, and T. W. Ebbesen, *Science* **363**, 615 (2019).
- [2] A. D. Dunkelberger, B. T. Spann, K. P. Fears, B. S. Simpkins, and J. C. Owrutsky, *Nat. Commun.* **7**, 13504 (2016).
- [3] K. Liu, G. Huang, X. Li, G. Zhu, W. Du, and T. Wang, *Adv. Mater.* **34**, 2109088 (2022).
- [4] M. Autore, P. N. Li, I. Dolado, F. J. Alfaro-Mozaz, R. Esteban, A. Atxabal, F. Casanova, L. E. Hueso, P. Alonso-Gonzalez, J.

Aizpurua, A. Y. Nikitin, S. Velez, and R. Hillenbrand, *Light. Sci. Appl.* **7**, 17172 (2018).

- [5] G. Dayal, I. Morichika, and S. Ashihara, *J. Phys. Chem. Lett.* **12**, 3171 (2021).
- [6] P. Xie, Y. Y. Wu, Y. H. Li, P. J. Chang, H. Zhang, and W. Wang, *J. Opt.* **24**, 093001 (2022).
- [7] L. J. Huang, A. Krasnok, A. Alu, Y. L. Yu, D. Neshev, and A. E. Miroshnichenko, *Rep. Prog. Phys.* **85**, 046401 (2022).

- [8] P. Xie, D. Li, Y. Chen, P. Chang, H. Zhang, J. Yi, and W. Wang, *Phys. Rev. B* **102**, 115430 (2020).
- [9] P. Torma and W. L. Barnes, *Rep. Prog. Phys.* **78**, 013901 (2015).
- [10] A. Shalabney, J. George, J. Hutchison, G. Pupillo, C. Genet, and T. W. Ebbesen, *Nat. Commun.* **6**, 5981 (2015).
- [11] J. P. Long and B. S. Simpkins, *ACS Photon.* **2**, 130 (2015).
- [12] W. Ahn, I. Vurgaftman, A. D. Dunkelberger, J. C. Owrutsky, and B. S. Simpkins, *ACS Photon.* **5**, 158 (2018).
- [13] B. Xiang, R. F. Ribeiro, Y. M. Li, A. D. Dunkelberger, B. B. Simpkins, J. Yuen-Zhou, and W. Xiong, *Sci. Adv.* **5**, eaax5196 (2019).
- [14] A. Bylinkin, M. Schnell, M. Autore, F. Calavalle, P. N. Li, J. Taboada-Gutierrez, S. Liu, J. H. Edgar, F. Casanova, L. E. Hueso, P. Alonso-Gonzalez, A. Y. Nikitin, and R. Hillenbrand, *Nat. Photonics* **15**, 197 (2021).
- [15] R. Hillenbrand, T. Taubner, and F. Keilmann, *Nature (London)* **418**, 159 (2002).
- [16] J. J. Greffet, R. Carminati, K. Joulain, J. P. Mulet, S. P. Mainguy, and Y. Chen, *Nature (London)* **416**, 61 (2002).
- [17] C. R. Gubbin, F. Martini, A. Politi, S. A. Maier, and S. De Liberato, *Phys. Rev. Lett.* **116**, 246402 (2016).
- [18] C. R. Gubbin, R. Berte, M. A. Meeker, A. J. Giles, C. T. Ellis, J. G. Tischler, V. D. Wheeler, S. A. Maier, J. D. Caldwell, and S. De Liberato, *Nat. Commun.* **10**, 1682 (2019).
- [19] A. M. Dubrovkin, B. Qiang, T. Salim, D. Nam, N. I. Zheludev, and Q. J. Wang, *Nat. Commun.* **11**, 1863 (2020).
- [20] P. N. Li, X. S. Yang, T. W. W. Mass, J. Hanss, M. Lewin, A. K. U. Michel, M. Wuttig, and T. Taubner, *Nat. Mater.* **15**, 870 (2016).
- [21] D. Yoo, F. de Leon-Perez, M. Pelton, I. H. Lee, D. A. Mohr, M. B. Raschke, J. D. Caldwell, L. Martin-Moreno, and S. H. Oh, *Nat. Photonics* **15**, 125 (2021).
- [22] W. L. Ma, G. W. Hu, D. B. Hu, R. K. Chen, T. Sun, X. L. Zhang, Q. Dai, Y. Zeng, A. Alu, C. W. Qiu, and P. N. Li, *Nature (London)* **596**, 362 (2021).
- [23] P. Xie, Q. Ding, Z. Liang, S. Shen, L. Yue, H. Zhang, and W. Wang, *Phys. Rev. B* **107**, 075415 (2023).
- [24] P. Xie, Y. H. Deng, L. X. Zeng, Z. C. Liang, S. Y. Shen, Q. Ding, H. Zhang, Z. K. Zhou, and W. Wang, *Phys. Rev. B* **106**, 165408 (2022).
- [25] P. Xie, Z. C. Liang, T. T. Jia, D. M. Li, Y. X. Chen, P. J. Chang, H. Zhang, and W. Wang, *Phys. Rev. B* **104**, 125446 (2021).
- [26] V. Kravtsov, E. Khestanova, F. A. Benimetskiy, T. Ivanova, A. K. Samusev, I. S. Sinev, D. Pidgayko, A. M. Mozharov, I. S. Mukhin, M. S. Lozhkin, Y. V. Kapitonov, A. S. Brichkin, V. D. Kulakovskii, I. A. Shelykh, A. I. Tartakovskii, P. M. Walker, M. S. Skolnick, D. N. Krizhanovskii, and I. V. Iorsh, *Light: Sci. Appl.* **9**, 56 (2020).
- [27] N. Bernhardt, K. Koshelev, S. J. U. White, K. W. C. Meng, J. E. Froch, S. Kim, T. Toan Trong, D.-Y. Choi, Y. Kivshar, and A. S. Solntsev, *Nano Lett.* **20**, 5309 (2020).
- [28] A. Elbanna, K. Chaykun, Y. Lekina, Y. Liu, B. Febriansyah, S. Li, J. Pan, Z. X. Shen, and J. Teng, *Opto-Electron. Sci.* **1**, 220006 (2022).
- [29] C. Fang, Q. Yang, Q. Yuan, X. Gan, J. Zhao, Y. Shao, Y. Liu, G. Han, and Y. Hao, *Opto-Electron. Adv.* **4**, 200030 (2021).
- [30] I. A. M. Al-Ani, K. As'Ham, L. J. Huang, A. E. Miroshnichenko, and H. T. Hattori, *Laser Photon. Rev.* **15**, 2100240 (2021).
- [31] M. B. Qin, J. Y. Duan, S. Y. Xiao, W. X. Liu, T. B. Yu, T. B. Wang, and Q. H. Liao, *Phys. Rev. B* **105**, 195425 (2022).
- [32] K. As'ham, I. Al-Ani, W. Lei, H. T. Hattori, L. J. Huang, and A. Miroshnichenko, *Phys. Rev. Appl.* **18**, 014079 (2022).
- [33] Z. T. Li, K. Cao, J. S. Li, Y. Tang, X. R. Ding, and B. H. Yu, *Opto-Electron. Adv.* **4**, 200019 (2021).
- [34] K. L. Sun, M. Sun, Y. J. Cai, U. Levy, and Z. H. Han, *Nanophotonics* **11**, 4221 (2022).
- [35] P. L. Hong, L. Xu, and M. Rahmani, *Opto-Electron. Adv.* **5**, 200097 (2022).
- [36] M. Shahzadi, C. Y. Zheng, S. Ahmad, S. S. Wang, and W. L. Zhang, *Opto-Electron. Adv.* **5**, 200066 (2022).
- [37] B. Lahiri, S. G. McMeekin, R. M. De La Rue, and N. P. Johnson, *Opt. Express* **21**, 9343 (2013).
- [38] K. S. Menghrajani, H. A. Fernandez, G. R. Nash, and W. L. Barnes, *Adv. Opt. Mater.* **7**, 1900403 (2019).
- [39] K. S. Menghrajani, G. R. Nash, and W. L. Barnes, *ACS Photon.* **6**, 2110 (2019).
- [40] K. Koshelev, S. Lepeshov, M. K. Liu, A. Bogdanov, and Y. Kivshar, *Phys. Rev. Lett.* **121**, 193903 (2018).
- [41] C. Zhou, S. Li, Y. Wang, and M. Zhan, *Phys. Rev. B* **100**, 195306 (2019).
- [42] S. Y. Shen, Y. Y. Wu, Y. H. Li, P. Xie, Q. Ding, X. Y. Kuang, W. X. Wang, and W. Wang, *Phys. Rev. B* **105**, 155403 (2022).
- [43] Z. C. Liang, L. Y. Qing, Z. J. Li, X. T. Nguyen, T. Xu, A. De Sio, H. Zhang, C. Lienau, and W. Wang, *Phys. Rev. B* **102**, 035422 (2020).
- [44] P. Vasa, R. Pomraenke, G. Cirmi, E. De Re, W. Wang, S. Schwieger, D. Leipold, E. Runge, G. Cerullo, and C. Lienau, *ACS Nano* **4**, 7559 (2010).
- [45] S. Zhang, H. Zhang, T. Xu, W. Wang, Y. Zhu, D. Li, Z. Zhang, J. Yi, and W. Wang, *Phys. Rev. B* **97**, 235401 (2018).
- [46] C. M. Savage and H. J. Carmichael, *IEEE J. Quantum Electron.* **24**, 1495 (1988).
- [47] C. Ropers, D. J. Park, G. Stibenz, G. Steinmeyer, J. Kim, D. S. Kim, and C. Lienau, *Phys. Rev. Lett.* **94**, 113901 (2005).
- [48] U. Akram, Z. Ficek, and S. Swain, *Phys. Rev. A* **62**, 013413 (2000).
- [49] P. Xie, Z. Liang, Z. Li, W. Wang, W. Wang, T. Xu, X. Kuang, L. Qing, D. Li, and J. Yi, *Phys. Rev. B* **101**, 045403 (2020).
- [50] Z. C. Liang, D. Wang, M. Ziegler, U. Hubner, P. Xie, Q. Ding, H. Zhang, and W. Wang, *Laser Photon. Rev.* **16**, 2200393 (2022).
- [51] W. Wang, P. Vasa, R. Pomraenke, R. Vogelgesang, A. De Sio, E. Sommer, M. Maiuri, C. Manzoni, G. Cerullo, and C. Lienau, *ACS Nano* **8**, 1056 (2014).
- [52] P. Vasa, W. Wang, R. Pomraenke, M. Lammers, M. Maiuri, C. Manzoni, G. Cerullo, and C. Lienau, *Nat. Photonics* **7**, 128 (2013).
- [53] P. Vasa, W. Wang, R. Pomraenke, M. Maiuri, C. Manzoni, G. Cerullo, and C. Lienau, *Phys. Rev. Lett.* **114**, 036802 (2015).
- [54] I. A. M. Al-Ani, K. As'Ham, L. J. Huang, A. E. Miroshnichenko, W. Lei, and H. T. Hattori, *Adv. Opt. Mater.* **10**, 2101120 (2022).